Rock Mech Rock Eng (2011) 44:199–210
DOI 10.1007/s00603-010-0104-7

ORIGINAL PAPER

# A Fully Coupled Chemo-Poroelastic Analysis of Pore Pressure and Stress Distribution around a Wellbore in Water Active Rocks

**Hamid Roshan · S. S. Rahman**

Received: 28 January 2010 / Accepted: 14 May 2010 / Published online: 1 June 2010


**Abstract** Water active rocks consist of minerals that hold water in their crystalline structure and in pore spaces. Free water from drilling fluid can be attracted by the formation depending on the potential differences between pore space and drilling fluid. The fluid movement into the formation or out of the formation can lead to a change in effective stress, thus causing wellbore failures. In all previous studies it is found that the solute transport from or to the formation is primarily controlled by diffusion process and the effect of advection on solute transfer is negligible for a range of very low permeable shale formations ($>10^{-5}$ mD). In this study a range of permeable shale formations ($10^{-5}$ to $10^{-3}$ mD) commonly encountered in drilling oil and gas wells are considered to investigate the solute transfer between drilling fluid and formation due to advection. For this purpose a finite element model of fully coupled chemo-hydro-mechanical processes was developed. Results of this study revealed that the solute transfer between the drilling fluid and the shale formation is controlled primarily by permeability of the shale formations. For the range of shale formations studied here, there exists a threshold permeability below which the solute transfer is dominated by diffusion process and above which by fluid in motion (fluid flow). Results from the numerical experiments have shown that when the permeability of shales is greater than this threshold permeability, the chemical potential gradient between the pore fluid and drilling fluid reaches equilibrium faster than that when the permeability of shales is below this threshold value. Also it has been found that when advection is taken into account, effective radial and tangential stresses decrease around the wellbore, particularly near the wellbore wall where the solute concentration has reached near equilibrium.

**Keywords** Chemo-poroelasticity · Advection · Water active rocks · Pore pressure · Stress distribution

H. Roshan · S. S. Rahman (✉)
School of Petroleum Engineering,
University of New South Wales, Sydney NSW2052, Australia
e-mail: sheik.rahman@unsw.edu.au

**List of symbols**

| | |
|---|---|
| $B$ | Skepmton coefficient |
| $C^{\mathrm{D}}$ | Average diluent mass fraction in formation |
| $C_{\mathrm{M}}$ | Average solute mass fraction in drilling fluid |
| $C_{\mathrm{S}}$ | Average solute mass fraction in formation |
| $D$ | Solute diffusion coefficient |
| $\vec{\vec{D}}_{\mathrm{e}}$ | Elastic modulus tensor |
| $G$ | Shear modulus of rock (second Lame's constant) |
| $\vec{\vec{k}}$ | Permeability tensor |
| $k_x$ | $x$-component of permeability tensor |
| $k_y$ | $y$-component of permeability tensor |
| $K_{\mathrm{f}}$ | Fluid bulk module |
| $K_{\mathrm{S}}$ | Solid bulk module |
| $M^{\mathrm{S}}$ | Molar mass of the solute |
| $N$ | Number of nodes |
| $N_P$ | Pressure shape functions |
| $N_u$ | Displacement shape functions |
| $N_C^{\mathrm{S}}$ | Mass fraction shape functions |
| $p$ | Pressure |
| $P_{\mathrm{i}}$ | Initial reservoir pressure |
| $P_{\mathrm{m}}$ | Drilling fluid pressure |
| $\vec{P}$ | Pore pressure vector |
| $R$ | Universal gas constant |
| $t$ | Time |
| $T$ | Absolute temperature |
| $T_{\mathrm{F}}$ | Formation temperature |
| $u$ | Displacement |

$\vec{U}$ Displacement vector
$\alpha$ Biot's Coefficient
$\zeta$ Variation of the fluid content
$\eta$ Coefficient of solute retardation
$\lambda$ First Lame's constant
$\mu$ Viscosity
$\nu$ Drained Poisson's ratio
$\nu_u$ Undrained Poisson's ratio
$\rho_f$ Fluid density
$\vec{\sigma}$ Stress tensor
$\sigma_h$ Minimum in situ horizontal stress
$\sigma_H$ Maximum in situ horizontal stress
$\phi$ Porosity
$\omega^S$ Chemical swelling parameter for solute
$\omega^D$ Chemical swelling parameters for diluent
$\Re$ Standard solute reflection coefficient

## 1 Introduction

The oil industry has been frustrated by its inability to effectively deal with wellbore instability problems, in particular when drilling through water-reactive shale formations (Zhang and Roegiers 2005). Problem with shale formation arises from two important mechanisms, namely crystalline swelling and chemical osmosis. Crystalline swelling is caused by the adsorption of mono-molecular layers of water on the basal crystal surface on both the external and, in the case of expanding lattices, the interlayer surfaces. The presence of counter ions on the surfaces of clay platelets causes an electrical diffuse layer to be formed. Thus, the presence of an electrical double layer (the fixed layer and diffusive layer) and the low permeability of shale constitute an osmotic behaviour which sustains chemical osmotic flow (Ghassemi and Diek 2003; Ghassemi and Tao 2009; Nguyen and Abousleiman 2009a). These characteristic properties of shale can be controlled by managing/manipulating the chemistry of drilling fluid (Van Oort and Hale 1996).

The effect of chemical osmosis on fluid flow has been investigated by several authors (Hanshaw and Zen 1965; Chenevert 1970; Mody and Hale 1993; Nguyen and Abousleiman 2009b). Sherwood (1993) developed a model to show the characteristic properties of shale and the presence of chemical osmotic flow between the pore space and the drilling fluid. The constitutive equations were derived from the difference in chemical potential between the pore fluid and the drilling fluid. Sherwood and Bailey (1994) extended their work to solve the plain strain solution for a cylindrical wellbore. The stress and pore pressure resulting from this solution are only valid for a hydrostatic stress field.

A complete set of constitutive equations for a fully coupled chemo-hydro-mechanical model for swelling of water active rocks was presented by Heidug and Wong (1996). They used a non-equilibrium thermodynamic approach based on an extended version of equations of poroelasticity and Darcy's Law. Also their model equations were able to show the effect of crystalline swelling as well as chemical osmotic flow. Ghassemi and Diek (1998, 2003) provided a set of analytical solutions for stability analysis of inclined wellbores.

Ekbote and Abousleiman (2006) used a different approach, which is based on the extended version of equations of poroelasticity and the work of Sherwood and Bailey (1994), to solve the problem of chemo-poroelasticity in transversely isotropic porous media and to describe the shales' mechanical behaviour. In all of the aforementioned work, solute transfer due to advection in low-permeable shale formations is assumed to be negligible.

In this paper, solute transfer due to advection in a range of permeable shales and its effect on change in pore pressure and stresses around the wellbore are investigated. The governing equations of chemo-poroelasticity are introduced and then their discretisation using finite element method is presented. Results of pore pressure and stress around the wellbore in a range of permeable shale formations are presented and discussed.

## 2 Governing Equations

Biot's (1941) poroelasticity has been extended to model the chemo-poroelasticity. The porous medium is assumed to consist of a porous solid matrix with elastic properties, where pore space is saturated by a fluid containing a number of chemical species. The chemical mechanism has the effects on pore pressure as well as mechanical deformation both of which are considered in the equations. Processes of mass transport involved in shale system studied here are presented in Table 1.

Governing equations of linear isothermal deformation of shale are based on the concept of free energy of a wetted clay matrix (Heidug and Wong 1996). The foundation is defined on a continuity equation for the difference in Helmholtz free energy between pore fluid and saturated

**Table 1** Direct and coupled flow phenomena in shales

| Flow/Force | Hydraulic gradient | Chemical potential gradient |
|---|---|---|
| Fluid | Hydraulic conduction Darcy's Law | Chemical osmosis |
| Solute (ion) | Advection | Modified Fick's law |

porous media under isothermal condition. To solve the Helmholtz free energy equation, the entropy production per unit volume of saturated porous media is calculated based on the theory of non-equilibrium thermodynamics. On the other hand, the alteration of fluid mass per unit volume and work done by solid deformation are treated as infinitesimal macroscopic transformation. The constitutive equations can be expressed as follows:

### 2.1 Navier Equations for Displacements

Momentum balance is employed to derive the Navier type equation for displacement:

$$G\nabla^2 u_i + \frac{G}{1-2v}e_i - \alpha' p_i + \omega_0 \chi a C_i^{\mathrm{S}} = 0 \tag{1}$$

where $G$ is shear module, $e = (\nabla u)$, $u$ is the rock displacement and $v$ is drained Poisson ratio.

### 2.2 Pressure Diffusion Equation

Using conservation of mass for a weakly compressible fluid along with the expression for the flux, one obtains a coupled fluid diffusion equation as

$$\alpha \dot{\varepsilon}_{ii} + \left(Q' + B'\right)\dot{P} + \beta\chi a \dot{C}^{\mathrm{S}} - \frac{k}{\mu}\nabla^2 p + \frac{k\Re\bar{\rho}_{\mathrm{f}} aRT}{\mu c M^{\mathrm{s}}}\nabla^2 C^{\mathrm{S}} = 0 \tag{2}$$

where $\alpha$ is the Biot's coefficient, $p$ is pore pressure, $k$ is absolute permeability, and $\mu$ is the fluid viscosity. $\varepsilon_{ii}$ and $C^{\mathrm{S}}$ are the components of total strain tensors and the solute mass fractions. Also $\Re$ is the standard solute reflection coefficient (or membrane efficiency), $T$ is the absolute temperature, $R$ is the universal gas constant and $M^{\mathrm{S}}$ is the molar mass of the solute. Time derivation of the parameters is presented with a dot.

### 2.3 Equation for Solute Diffusion

Conservation of mass of each chemical species in rock yields the following equation:

$$\phi\eta_j \dot{C}_j^{\mathrm{S}} + (1-\Re)\nabla\left(J_{\mathrm{f}} C_j^{\mathrm{S}}\right) - (1-\Re)D\nabla^2 C_j^{\mathrm{S}} = 0 \tag{3}$$

where $D$ is the solute diffusion coefficient, $J_{\mathrm{f}}$ is flux of fluid and $\eta_j$ is the retardation coefficient of each chemical species.

Using solute mass conservation law, $C^{\mathrm{s}}$ can be defined in terms of

$$C^{\mathrm{s}} = \sum C_j^{\mathrm{S}}$$

where $C_j^{\mathrm{S}}$ is the mass fraction of each chemical species which form the solute.

The coefficients in governing equations are:

$$\chi = \left(1 - \frac{C^{\mathrm{S}}_{\mathrm{mean}}}{C^{\mathrm{D}}_{\mathrm{mean}}}\right),\ c = C^{\mathrm{D}}_{\mathrm{mean}},\ a = \left(\frac{1}{C^{\mathrm{S}}_{\mathrm{mean}}}\right)$$

$$\alpha' = \left(\alpha - \frac{M^{\mathrm{S}}\omega_0}{cRT\bar{\rho}_{\mathrm{f}}}\right),\ \beta = \frac{\omega_0(\alpha-1)}{K},$$

$$B' = \frac{\omega_0(\alpha-1)}{K}\frac{M^{\mathrm{S}}}{cRT\bar{\rho}_{\mathrm{f}}}$$

$$Q' = \left(Q + \frac{\varphi}{K_{\mathrm{f}}}\right),\ Q = \frac{(\alpha-\varphi)}{K_{\mathrm{S}}}$$

where $C^{\mathrm{D}}_{\mathrm{mean}}$ and $C^{\mathrm{S}}_{\mathrm{mean}}$ are the average initial mass fraction of diluent and solute in shale formation. $K_{\mathrm{f}}$, $K_{\mathrm{S}}$, $\phi$ and $\bar{\rho_{\mathrm{f}}}$ are fluid bulk module, solid bulk module, porosity, and fluid density, respectively. The chemo-mechanical parameter, $\omega$, also known as chemical swelling parameter, can be defined as follows:

$$\omega^{\mathrm{S}} = \omega^{\mathrm{D}} = \omega_0 \frac{M^{\mathrm{S}}}{RT}$$

For details, readers can refer to Appendix A.

## 3 Finite Element Discretisation and Solution Strategy

### 3.1 Finite Element Discretisation

The technique presented by Zienkiewicz and Taylor (2000) is used to discretise the governing equations of chemo-poroelasticity (Eqs. 1, 2 and 3) which resulted in the following coupled non linear system of equation:

$$\begin{bmatrix} K & A & -W \\ A^T & -(\mathrm{S} + \Delta t H_{\mathrm{H}}) & -\left(\overset{\wedge}{M} + \Delta t D_{\mathrm{H}}\right) \\ 0 & 0 & -(M + \Delta t D_{\mathrm{D}}) \end{bmatrix} \begin{bmatrix} \overrightarrow{\Delta U_i} \\ \overrightarrow{\Delta P_i} \\ \overrightarrow{\Delta C_i^{\mathrm{S}}} \end{bmatrix} = \begin{bmatrix} \Delta f \\ \Delta t H_{\mathrm{H}} p(t_{i-1}) + \Delta t D_{\mathrm{H}} C^{\mathrm{S}}(t_{i-1}) \\ \Delta t D_{\mathrm{D}} p(t_{i-1}) \end{bmatrix} \tag{4}$$

where $i$ is the time step; $\vec{P}$ is the pore pressure vector; $\vec{P}_T = (p_1 \quad p_2 \quad \ldots \quad p_n)$; $p$ is the nodal pore pressure; $n$ is the number of nodes; $\overrightarrow{C}$ is the solute mass fraction vector; $\overrightarrow{C}_T = \left(C_1^{\mathrm{S}} \quad C_2^{\mathrm{S}} \quad \ldots \quad C_n^{\mathrm{S}}\right)$; $c^{\mathrm{S}}$ is the nodal solute mass fraction; $n$ is the number of nodes; $\vec{U}$ is the displacement vector; $\vec{U}_T = (u_{x1} \quad u_{y1} \quad u_{x2} \quad \ldots \quad u_{yn})$; $u_x$ is the nodal value of $x$-component of displacement, $u_y$ is the nodal value of $y$-component of displacement; $\overrightarrow{\Delta P} = \vec{P}_i - \vec{P}_{i-1}$; $\overrightarrow{\Delta U} = \vec{U}_i - \vec{U}_{i-1}$; $\overrightarrow{\Delta C^{\mathrm{S}}} = \overrightarrow{C_i^{\mathrm{S}}} - \overrightarrow{C_{i-1}^{\mathrm{S}}}$ and $\Delta t$ represents the time increment. Additionally, $\vec{\vec{W}}, \vec{\vec{H}}_{\mathrm{H}}, \vec{\vec{A}}, \vec{\vec{K}}, \overset{\wedge}{\vec{\vec{M}}}, \vec{\vec{D}}_{\mathrm{D}}, \vec{\vec{M}}, \vec{\vec{D}}_{\mathrm{H}}$ and $\overrightarrow{\vec{\mathrm{S}}}$ are the matrices defined in the Appendix B.

### 3.2 Solution Strategy

A finite element code is developed to solve the non-linear Eq. 4. First, the change in mass fraction of each chemical species (cations and anions) is obtained using previous nodal pore pressure by characteristic Galerkin discritisation method. Next, the results of mass fractions of chemical species are added up to form the mass fraction of solute. Then pore pressure and solid displacement are solved simultaneously for current time step based on solute mass fractions which was obtained from the previous step. A direct iteration technique is employed to simultaneously solve for nodal solid displacement, pore pressure, and solute mass fraction for current time step. An exact solution is obtained for defined convergence accuracy. This procedure is repeated for every time step.

## 4 Model Description and Validation

Model geometry includes a wellbore and its surrounding formation. Spatial discretisation (FEM mesh) of the model geometry is presented in Fig. 1. Note that only a quarter of the model is discretised by taking advantage of symmetry. The two-dimension isoparametric quadrilateral elements are chosen for this purpose. The inner and outer radii of model geometry are 0.1 and 10 m, respectively. In order to obtain maximum accuracy from a numerical scheme, mesh size is reduced to 10 m and the number of elements increased to over 500. The maximum ($\sigma_H$) and minimum ($\sigma_h$) horizontal stresses are aligned with the $x$ and $y$ axes, respectively. 8-noded isoparametric quadrilateral elements for solid displacement and 4-noded ones for pore pressure and solute mass fraction are used.

A full range of chemo-hydro-mechanical properties of shale is not commonly available. A set of reference data for shale, pore fluid, solute, and drilling fluid used in this study are summarised in Table 2 (Van Oort and Hale 1996; Ghassemi and Diek 2003; Ghassemi and Tao 2009). The permeability of the formation is varied from $10^{-5}$ to $10^{-3}$ mD and retardation coefficients are chosen 1 and 18.52 for $Cl^-$ and $Na^+$, respectively (Shackelford 1990; Muhammad 2004). For all the numerical experiments, the chemo-hydro-mechanical properties of shale mentioned in Table 2 are used unless otherwise stated.

When a well is drilled in low-permeable fluid-saturated rocks, fluid is initially trapped inside the pores. Thus, any pore deformation caused by change in stress field results in a change in pore pressure accordingly. In other words, pore fluid undergoes the same strain as that of pore matrix (Rice and Cleray 1976; Detournay and Cheng 1988). This phenomenon is called undrained response. Rock behaves as a stiffer material under this condition than that in drained condition. Pore pressure dissipates by diffusive transport of flow until drained condition is reached. The transition time for the dissipation of pore pressure is a function of

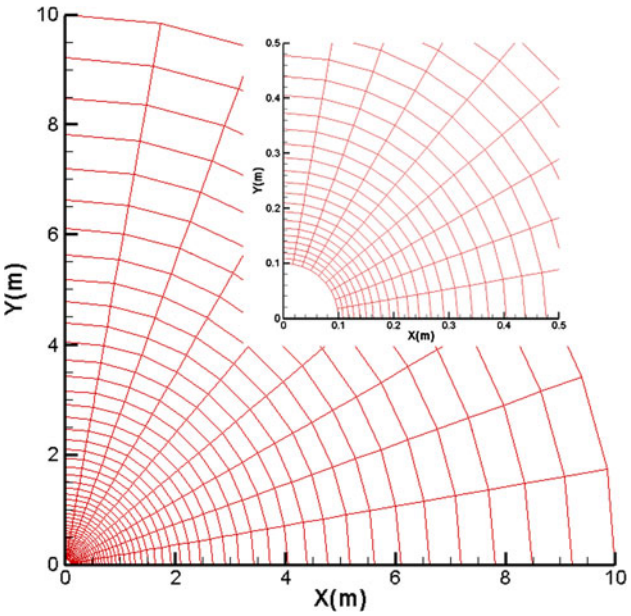


**Fig. 1** Spatial discretisation (FEM mesh) of the model geometry

**Table 2** Input data

| | |
|---|---|
| Mechanical parameters | |
| Drained Poisson's ratio ($\nu$) | 0.219 |
| Undrained Poisson's ratio ($\nu_u$) | 0.461 |
| Skempton coefficient ($B$) | 0.915 |
| Swelling coefficient ($\omega_o$) | 10 MPa |
| Bulk Young's modulus ($E$) | 4.4 GPa |
| Maximum horizontal stress ($\sigma_H$) | 23 MPa |
| Minimum horizontal stress ($\sigma_h$) | 20 MPa |
| Solid bulk module ($K_S$) | 77.5 GPa |
| Hydraulic parameters | |
| Drilling fluid pressure ($P_m$) | 12 MPa |
| Initial reservoir pressure ($P_i$) | 10 MPa |
| Fluid bulk module ($K_f$) | 2.5 GPa |
| Chemical parameters | |
| Average solute mass fraction in formation ($C_f$) | 0.1 |
| Average solute mass fraction in drilling fluid ($C_m$) | 0.2 |
| Molar mass of solute, $M^S$ (NaCl) | 0.0585 kg/mol |
| Solute diffusion coefficient ($D$) | $5 \times 10^{-9}$ m$^2$/s |
| Membrane efficiency or reflection coefficient ($\Re$) | 0.1 |
| Physical parameters | |
| Formation temperature ($T_F$) | 385°K |
| Wellbore radius ($r_w$) | 0.1 m |
| Fluid viscosity ($\mu$) | $3 \times 10^{-4}$ Pa s |
| Fluid density ($\rho^-$) | 1,111.11 kg/m$^3$ |
| Porosity ($\phi$) | 0.143 |

formation permeability. Therefore, undrained response is considered here to capture the real change in pore pressure and stress distribution. The undrained response to isotropic loading causes no bulk deformation. Thus, the pore pressure remains drained. When the loading is deviatoric, the pore fluid and bulk share the load thus causing a change in pore pressure in different directions (Detournay and Cheng 1988; Hodge 2006). In order to capture the change in pore pressure the anisotropic state of stress is used in this study. Superconvergent patch recovery method (Zienkiewicz and Zhu 1992; Boroomand and Zienkiewicz 1997) is used to evaluate nodal stress tensors from the numerical results of nodal displacement.

It is assumed that the compressive stress is positive and tensile stress negative. The rock is considered as a homogenous porous medium. Plane strain hypothesis and instantaneous drilling are used to solve Eq. 4. The solution of Eq. 4 requires knowledge of initial solute concentration and pore pressure within the flow domain:

$$C_j^{\mathrm{S}}(x,y,t) = C_{j\mathrm{mean}}^{\mathrm{S}}(x,y) \quad \text{for } t = 0$$

$$P(x,y,t) = P_i(x,y) \quad \text{for } t = 0$$

Dirichlet type boundary condition is applied to the inner boundary for the solute concentration and pore pressure as follows:

$$C_j^{\mathrm{S}}(x,y,t) = C_{j1}^{\mathrm{S}}(x,y,t) \text{ on boundary}$$

$$P(x,y,t) = P_1(x,y,t) \text{ on boundary}$$

where $P_1$ and $C_{j1}^{\mathrm{S}}$ are the known functions of time and space at all points of the specific boundary.

In this study the effect of plasticity on porous solid matrix deformation is ignored. Also the current model is limited to 2D and homogenous porous medium, and the effect of temperature on the electro-chemical, physical, and mechanical properties are not considered.

Numerical results are validated with appropriate analytical solutions presented by Ghassemi and Diek (2003) and Ekbote and Abousleiman (2006). In order to verify the results of solute mass fraction due to advection analytical solutions, which are presented by Zoppou and Knight (1997) are used. In Figs. 2, 3, 4 and 5 the distribution of solute mass fraction, change in pore pressure, the distribution of effective radial and tangential stresses around the wellbore are presented at different times: 30 min, 7 h, and 47 h. Also in Fig. 6 the change in solute mass fraction by advection is presented. A good agreement can be observed between analytical and numerical solutions. Chemo-hydro-mechanical properties for shale formation, pore fluid, solute, and drilling fluid used for validation of the model are presented in Table 2. The formation permeability and retardation coefficient used for this purpose are $10^{-3}$ mD and 1, respectively. Also the solute mass fraction of shale

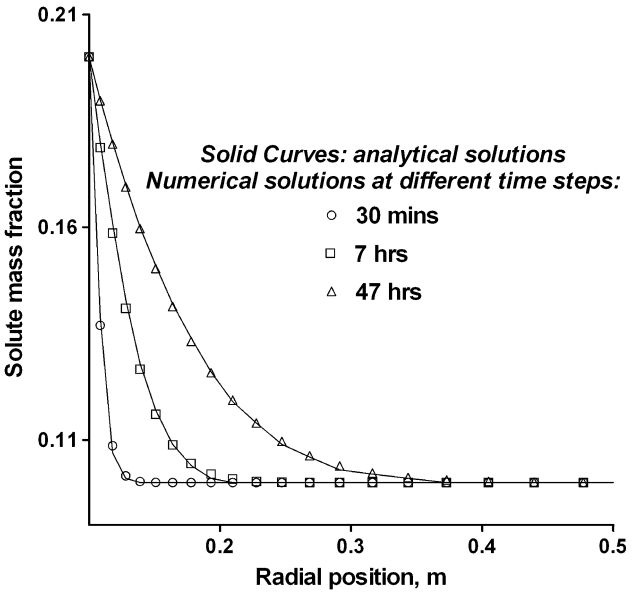


**Fig. 2** Solute mass fraction distribution based on analytical and numerical solutions at different time steps: 30 min, 7 h, and 47 h

formation ($C_{\mathrm{S}}$) and drilling fluid ($C_{\mathrm{m}}$) are considered 0.0 and 0.2, respectively, to validate the solute mass fraction by diffusion–advection.

## 5 Numerical Results and Discussion

The undrained response of low-permeable rocks such as shale plays an important role in wellbore stability. When a well is drilled in low-permeable fluid-saturated rocks, fluid is initially trapped inside the pores. Any pore deformation caused by change in stress field results in a change in pore pressure. In Fig. 7 the effect of undrained response on pore pressure in early (10 min) and late (13.7 h) times are presented. As expected, the early pressure drops along $x$ and $y$ axes are not the same due to undrained response resulting from the difference between the two major horizontal stresses. As time progresses, fluid moves through the pores, thus causing it to change from undrained to a drained condition.

According to the industry-wide practice the water salinity of drilling fluid is kept higher than that of pore fluid ($C_{\mathrm{m}} > C_{\mathrm{f}}$) to avoid wellbore instability. In the case where the water salinity of drilling fluid is less than that of pore fluid, drilling fluid moves towards the formation due to hydraulic and chemical osmotic flow, thus increasing the pore pressure around the wellbore which often leads to a rapid wellbore failure.

In Fig. 8, the results of the effect of permeability on solute transfer are presented. In this study very low to medium permeability of shale formations are considered:

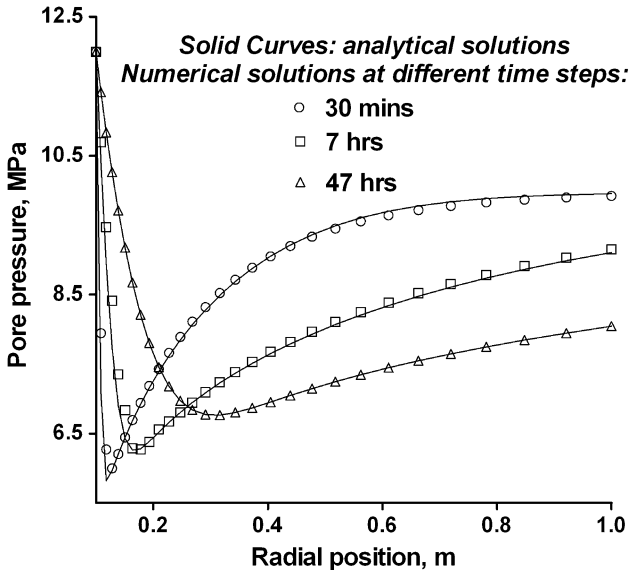


**Fig. 3** Pore pressure distribution based on analytical and numerical solutions at different time steps: 30 min, 7 h, and 47 h

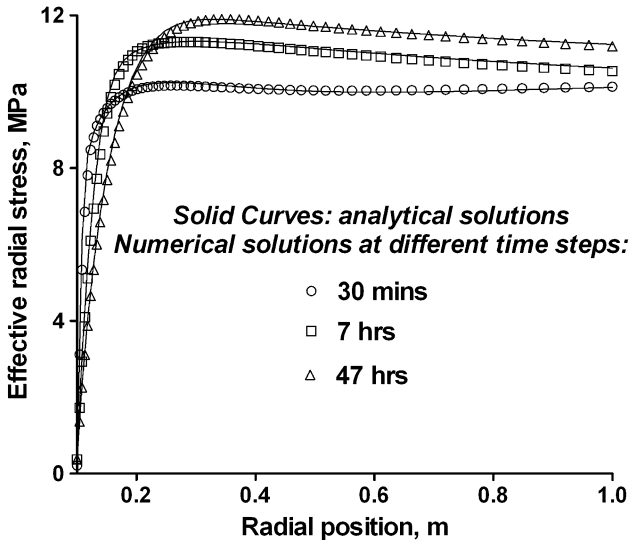


**Fig. 4** Effective radial stress along *x*-axis based on analytical and numerical solutions at different time steps: 30 min, 7 h, and 47 h

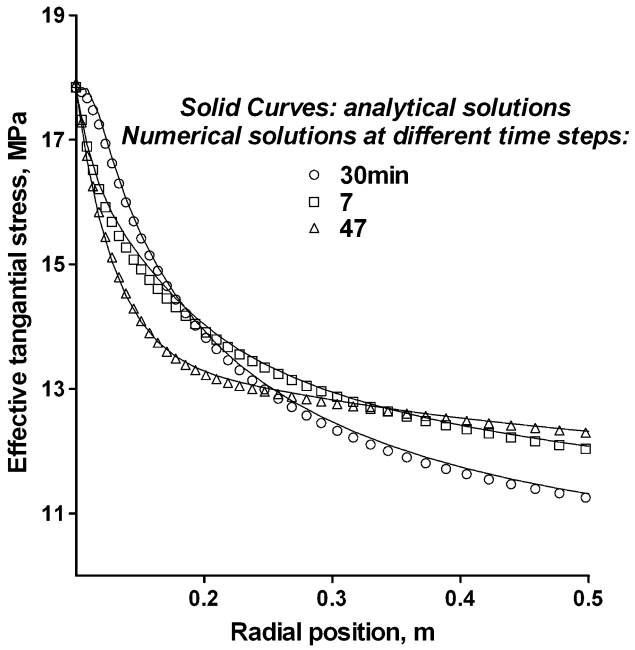


**Fig. 5** Effective tangential stress along *x*-axis based on analytical and numerical solutions at different time steps: 30 min, 7 h, and 47 h

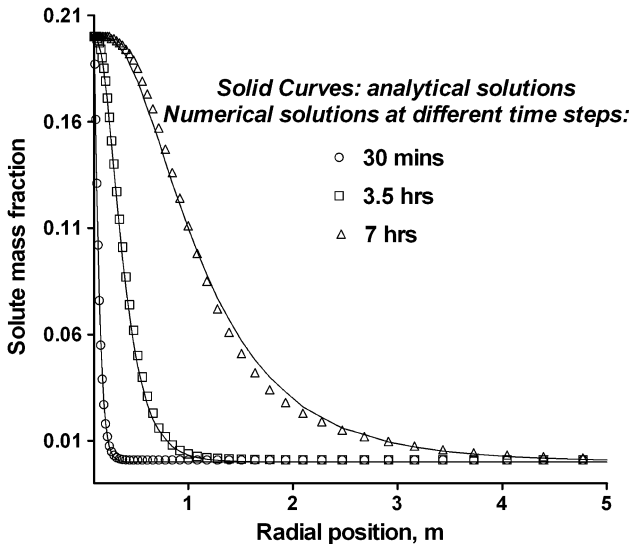


**Fig. 6** Solute mass fraction distribution based on analytical solutions (*solid lines*) and numerical solutions at different time steps: 30 min, 7 h, and 47 h

$10^{-5}$, $10^{-4}$, and $10^{-3}$ mD. Chemo-hydro-mechanical parameters used in this study are presented in Table 2. From the results of this study it can be observed that there exists a threshold permeability ($10^{-4}$ mD) for a combination of parameters used in the current numerical experiments. It can be seen from Fig. 8 that for permeabilities less than $10^{-4}$ mD the plot of solute mass fraction with radial position at 1.7 h with advection overlaps with the plot of that without advection (diffusion). This means, when the permeability of shale formations is lower than $10^{-4}$ mD, solute mass transfer takes place only due to diffusion of salts. In the case where permeability is higher than $10^{-4}$ mD, a significantly high amount of solute is transported to the shale formation. This solute transport is caused by a combination of hydraulic flow and chemical osmotic flow. It can also be seen that the solute transfer is a function of time. With pass of time more solute is transported through the shale formations.

Results of the effect of reflection coefficient and retardation coefficient on solute transfer for 13.7 h are presented in Figs. 9, 10 and 11. In this study permeabilities of

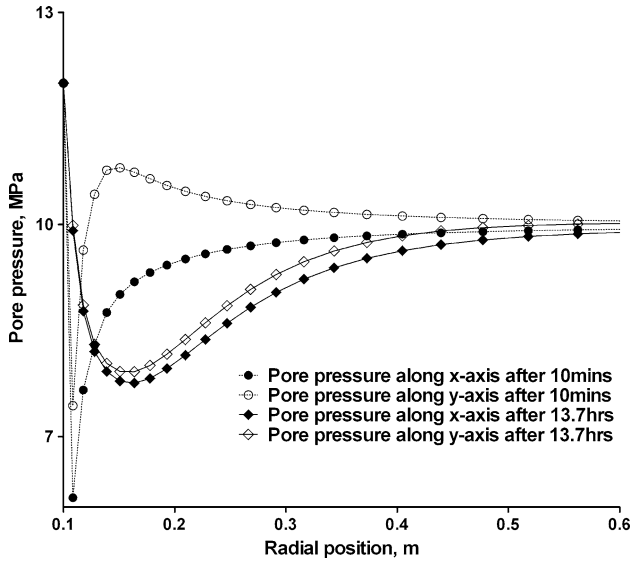


**Fig. 7** Pore pressure distribution along $x$ and $y$ axis at different time steps in shale formation with permeability of $10^{-4}$ mD

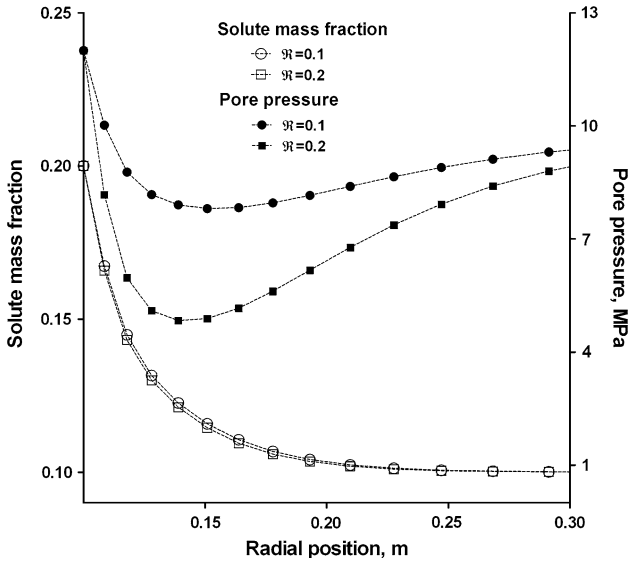


**Fig. 9** Distribution of solute mass fraction and pore pressure in shale formation with permeability $10^{-5}$ mD for two different reflection coefficients, $\Re$ 0.1 and 0.2 at 13.7 h

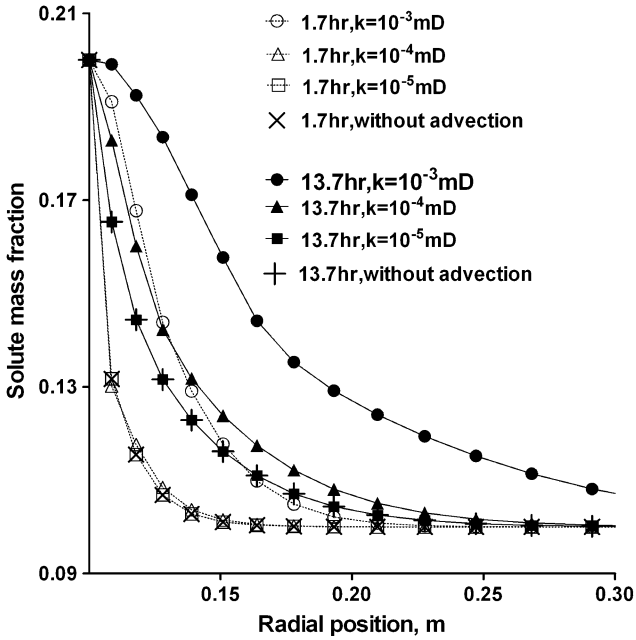


**Fig. 8** Distribution of solute mass fraction with and without advection after 13.7 h in shale formation with three different permeabilities: $10^{-5}$, $10^{-4}$, and $10^{-3}$ mD

shale formation are considered $10^{-3}$ and $10^{-5}$ mD and reflection coefficients $\Re = 0.1$ and 0.2, respectively. For low-permeable shale formation ($10^{-5}$ mD) solute transfer from the wellbore to the formation decrease with increase in reflection coefficient; consequently, formation pressure decreases. At the radial position 0.3 m this decrease in pressure amounts to about 1 MPa (see Fig. 9). In high-permeable shale formation ($10^{-3}$ mD) one can observe from Fig. 10 that the solute transport from the wellbore to the formation increases with increase in reflection coefficient. Increase in reflection coefficient, however, decreases the formation pressure, and this decrease is lower in high-permeable shale formation than that in low permeable shale formation. The increase in solute transfer from the wellbore to high-permeable shale formation with increase in reflection coefficient is primarily due to advection.

In Fig. 11 the effect of retardation coefficient on solute transfer for two cases, with and without retardation coefficient, at different times is presented. In this study, permeability of shale formation is considered $10^{-3}$ mD and the retardation coefficient, $\eta$ is 18.52 for $Na^+$ and 1 for $Cl^-$. It can be seen from this figure that as the retardation coefficient increases the solute transfer through the shale formation decreases. This is due to absorption of ions on the rock surface.

In order to investigate the effect of advection on pore pressure two cases are considered: with and without advection. In this study shale formation with two permeabilities: $10^{-5}$ and $10^{-3}$ mD at two different times: an early time 1.7 h and a late time 13.7 h, respectively, are considered. Results of this study are presented in Figs. 12 and 13. From this result it can be seen that there is a sharp pressure drop near the wellbore wall in particular at early time. With the pass of time pore pressure near the wellbore wall increases. Pressure drop near the wellbore wall in low-permeable shale, however, is much greater than that in high-permeable shale. This can be explained by the fact that due to osmotic flow fluid is drawn out of the formation resulting in a pressure drop. In high-permeable formation, however, pressure drop is less because solute is transported from the wellbore to the formation due to advection, thus compensating a part of the

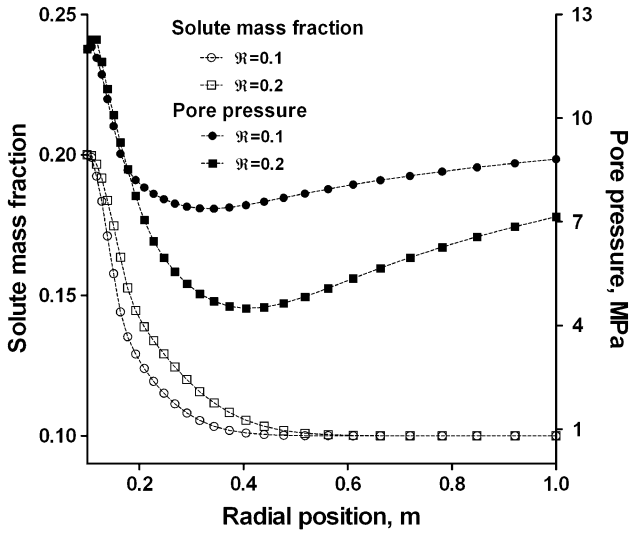


**Fig. 10** Distribution of solute mass fraction and pore pressure in shale formation with permeability $10^{-3}$ mD for two different reflection coefficients, ℜ 0.1 and 0.2 at 13.7 h

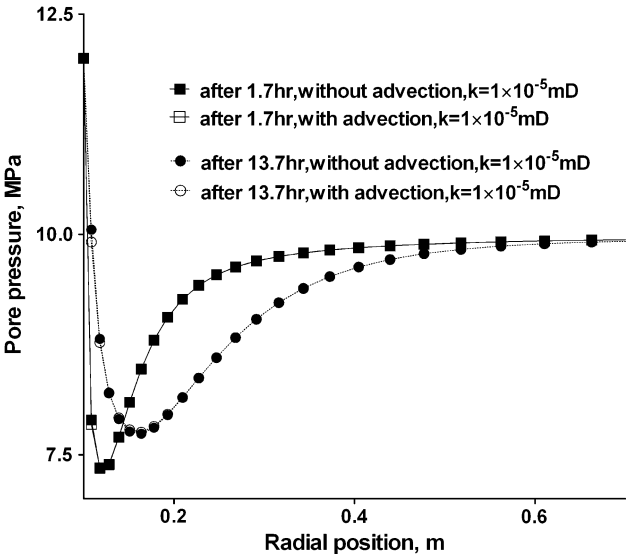


**Fig. 12** Pore pressure distribution around the wellbore in shale formation with permeability of $10^{-5}$ mD at two different time steps: 1.7 and 13.7 h

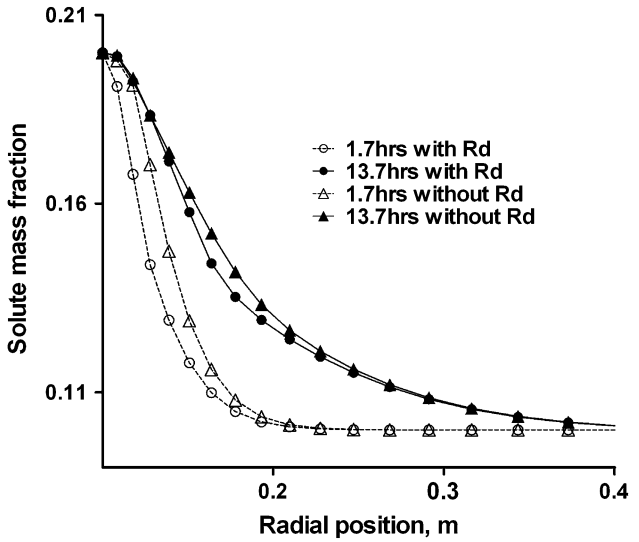


**Fig. 11** Distribution of solute mass fraction at two different time steps: 1.7 and 13.7 h with and without the effect of retardation coefficient on solute transfer

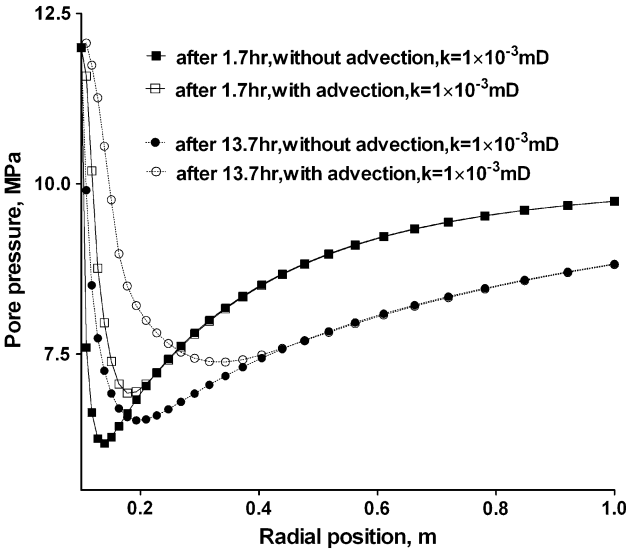


**Fig. 13** Pore pressure distribution around the wellbore in shale formation with permeability of $10^{-3}$ mD at two different time steps: 1.7 and 13.7 h

pressure drop caused by osmotic flow. From Fig. 13 it can be also seen that when advection is not considered a pressure of 5.75 MPa occurs at radial position of 0.14 m after 1.7 h. When solute transfer due to advection is considered, the formation pressure becomes 7.5 MPa at the same radial position and the same time (1.7 h). Similar observation can be made for the 13.7 h time step.

In order to show the effect of advection on stresses around the wellbore two cases are considered: with and without advection. Change in solute mass fraction around the wellbore can affect the stress distribution by two mechanisms: chemical osmosis and crystalline swelling of shale matrix. In Figs. 14 and 15 the effective radial stresses along $x$ and $y$ axes after 13.7 h for two different permeable shale formations of $10^{-3}$ and $10^{-5}$ mD for both cases, with and without advection, are presented. From these figures it can be seen that when advection is taken into account, effective radial stress decreases around the wellbore, particularly near the wellbore wall, where the solute concentration has almost reached the equilibrium (see Fig. 8, for shale formation permeability of $10^{-3}$ mD after 13.7 h). From Fig. 14 it can be observed that advection has no

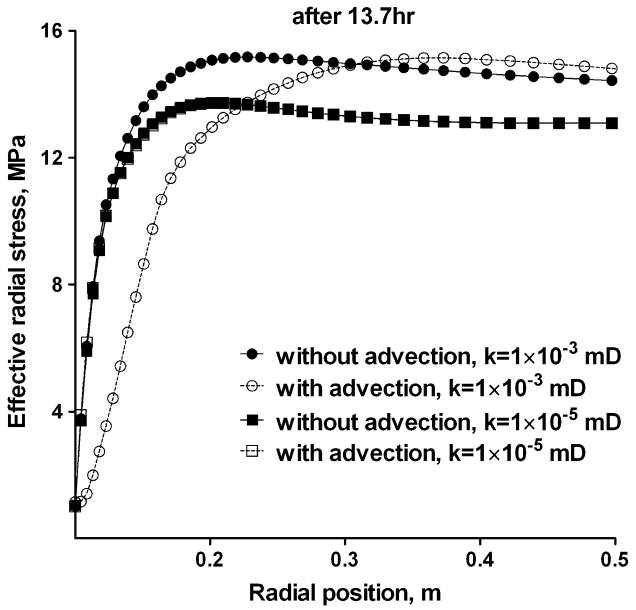


**Fig. 14** Effective radial stress distribution along $x$-axis after 13.7 h in shale formation with two different permeabilities: $10^{-5}$ and $10^{-3}$ mD

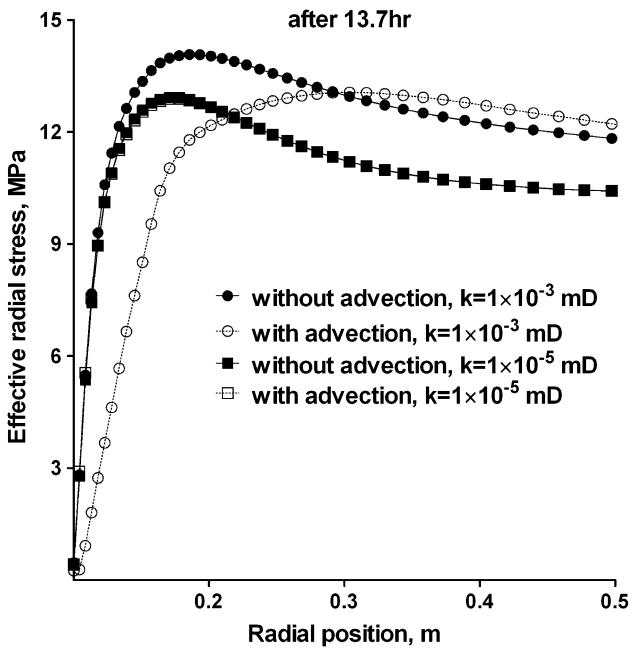


**Fig. 15** Effective radial stress distribution along $y$-axis after 13.7 h in shale formation with two different permeabilities: $10^{-5}$ and $10^{-3}$ mD

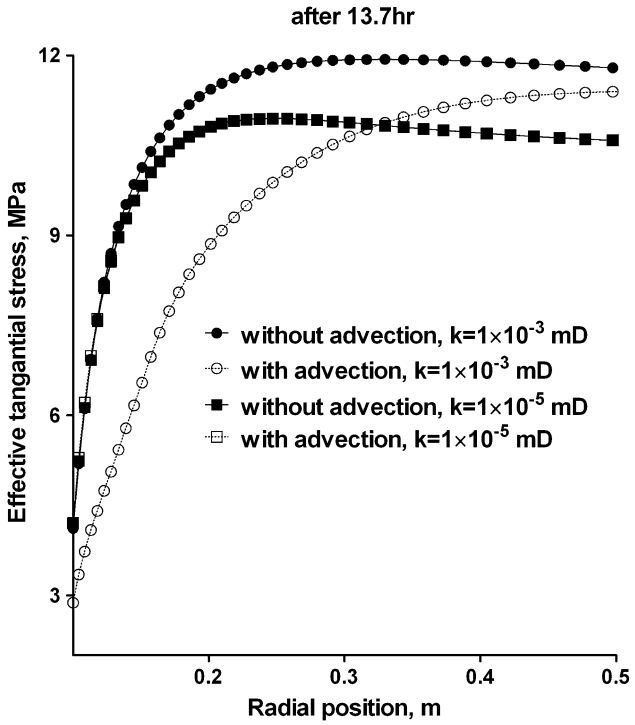


**Fig. 16** Effective tangential stress distribution along $x$ axis after 13.7 h in shale formation with two different permeabilities: $10^{-5}$ and $10^{-3}$ mD

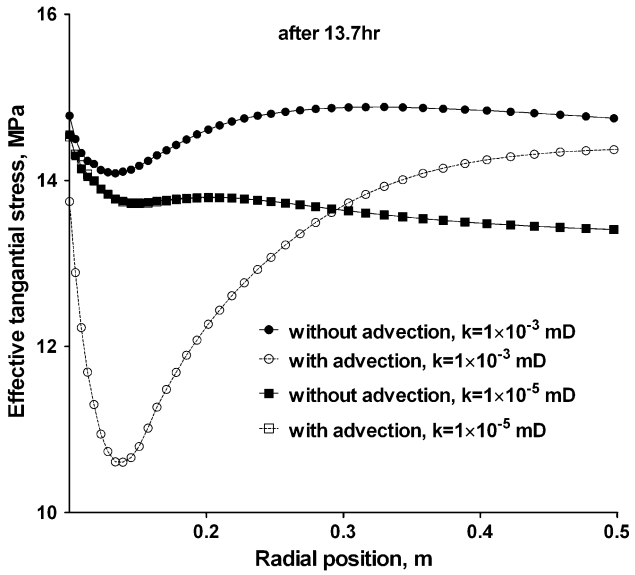


**Fig. 17** Effective tangential stress distribution along $y$ axis after 13.7 h in shale formation with two different permeabilities: $10^{-5}$ and $10^{-3}$ mD

effect on radial stress for formation with permeabilities less than $10^{-4}$ mD. When the permeability is increased to $10^{-3}$ mD, a decrease in radial stress by 20% is observed.

In Figs. 16 and 17 the effective tangential stresses along $x$ and $y$ axes after 13.7 h for both cases, with and without advection, is presented. These figures confirm that wells in formation with permeability greater than $10^{-4}$ mD are likely to experience lower tangential stress at the wellbore wall. This can be explained by two mechanisms, chemical osmosis and crystalline swelling, of shale matrix. When the advection is considered the pressure drop is lower around the wellbore than that of without advection. Thus, the effective stresses decrease with increase in pore pressure

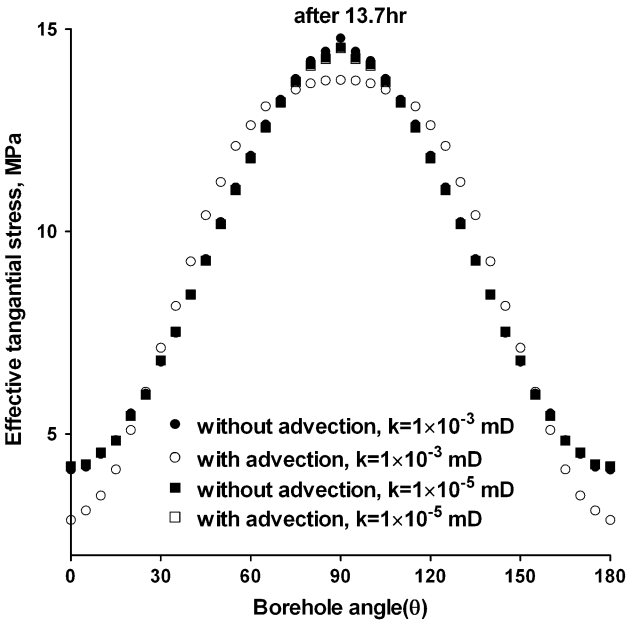


**Fig. 18** Effective tangential stress distribution along the circumference of the wellbore

(due to advection). Also high solute transport to the formation due to advection causes the matrix to swell (crystalline swelling), thus decreasing the effective tangential stress near wellbore region.

In Fig. 18, the effective tangential stress distribution with varying azimuth angle around the wellbore at the wellbore wall after 13.7 h is presented. From this figure one can observe that the tangential stress is lower by 1.5 MPa for permeability of $10^{-3}$ mD than that for $10^{-5}$ mD. This means that the solute transport by advection and consequent change in stress has the potential to induce tensile failure at wellbore wall.

## 6 Conclusion

In this paper the effect of advection on solute transport and consequent change in pore pressure and stress distribution around the wellbore drilled in water active shales is studied with the use of a numerical fully coupled chemo-poro-elastic model. In this study $C_m > C_S$ is considered as this is an industry-wide practice to maintain a stable wellbore.

From the numerical results it was revealed that the solute transfer from the fluid to the formation increases due to advection and that the solute transfer is faster for advection-dominated process than that for diffusion-dominated process only. Thus, chemical equilibrium can be reached sooner due to advection which makes the chemical osmosis disappear. When the diffusion dominates the solute transfer process, chemical osmosis can be sustained over a longer period of time.

It was also found that the state of stresses around the wellbore can be significantly altered by the advection of solute. When advection is considered the tangential stresses at the wellbore wall is likely to be tensile. Also effective radial stress can be seen to decrease near the wellbore wall.

## Appendix A

### Rock Constitutive Equations

The fluid saturated porous medium is composed of the solid matrix which contains two kinds of connected voids of different scales: pore space filled with freely diffusing pore fluid and interlayer space occupied by bounded water between individual clay plates. Solid structure of porous medium is assumed to be linearly elastic material, saturated with a binary electrolyte solution, which swells/shrinks in response to variations in the chemical potential of the diluent and solute components. The fundamental constitutive equations for change in stress state and pore pressure are derived from the free energy density of the wetted mineral matrix containing bound fluid proposed by Heidug and Wong (1996).

$$\dot{\sigma_{ij}} = \left(K - \frac{2G}{3}\right)\dot{\varepsilon_{kk}}\,\delta_{ij} + 2G\,\dot{\varepsilon_{ij}} - \alpha'\,\dot{p}\,\delta_{ij} + \omega_0\chi a\,\dot{C^{S}}\,\delta_{ij} \tag{5}$$

$$\dot{\zeta} = \alpha\,\dot{\varepsilon_{ii}} + \left(Q' + B'\right)\dot{p} + \beta\chi a\,\dot{C^{S}} \tag{6}$$

where $K$, $G$ are bulk and shear moduli. $\alpha$, Biot's coefficient can be defined as follows: $\alpha = \frac{3(\nu_u - \nu)}{B(1-2\nu)(1+\nu_u)}$. Also $\dot{\sigma_{ij}}$ and $\dot{\varepsilon_{ij}}$ are the components of the total stress and strain tensors differentiating based on time. $p$ is pore pressure and $\zeta$ is the variation of the fluid content (per unit referential volume) and the solute and diluent mass fractions are $C^S$ and $C^D$, respectively. The chemo-mechanical parameter $\omega$ which is the chemical swelling parameter can be defined as follows:

$$\omega^S = \omega^D = \omega_0\frac{M^S}{RT}$$

The coefficients are:

$$\chi = \left(1 - \frac{C^S_{mean}}{C^D_{mean}}\right), c = C^D_{mean}, a = \left(\frac{1}{C^S_{mean}}\right)$$

$$\alpha' = \left(\alpha - \frac{M^S\omega_0}{cRT\,\bar{\rho}_f}\right), \beta = \frac{\omega_0(\alpha - 1)}{K},$$

$$B' = \frac{\omega_0(\alpha - 1)}{K}\,\frac{M^S}{cRT\,\bar{\rho}_f}$$

$$Q' = \left(Q + \frac{\phi}{K_f}\right), Q = \frac{(\alpha - \phi)}{K_S}$$

where $T$ is the absolute temperature, $R$ is the universal gas constant, $M^{\mathrm{S}}$ is the molar mass of the solute. Also $K_{\mathrm{f}}$, $K_{\mathrm{S}}$, $\phi$, and $\bar{\rho}_{\mathrm{f}}$ are fluid bulk module, solid bulk module, porosity, and fluid density, respectively.

Transport Equations

Here, the phenomenological equations relating the fluxes to their driving forces are derived from the definition of Rayleigh dissipation function and the generalised forces associated with that. The driving forces form the several direct and coupled flows inside the water active rocks. Direct flows are in the form of hydraulic conduction and direct solute diffusion, whereas coupled flows are in the form of chemical osmosis and advection. As can be seen in Table 1 (Bader and Kooi 2005) four types of flows are considered to form this work. The phenomenological equations relating the thermodynamic driving forces to the fluid $J_{\mathrm{f}}$ and chemical species of solute $J_{j\mathrm{s}}$ fluxes they produce may be written, respectively, as

$$J_{\mathrm{f}} = -\frac{\bar{\rho}_{\mathrm{f}} k}{\mu}\left(\nabla p - \frac{\bar{\rho}_{\mathrm{f}} \Re a R T}{c M^{\mathrm{S}}}\nabla C^{\mathrm{S}}\right) \tag{7}$$

$$J_{j\mathrm{s}} = \bar{\rho}_{\mathrm{f}}(1-\Re) J_{\mathrm{f}} C_j^{\mathrm{S}} - \bar{\rho}_{\mathrm{f}}(1-\Re) D \nabla C_j^{\mathrm{S}} \tag{8}$$

where $\Re$ is the standard solute reflection coefficient (or membrane efficiency) and $D$ is the solute diffusion coefficient.

Governing (Field) Equations

*Navier Equations for Displacements*

Substituting Eq. 5 into the momentum balance equation, one obtains the first three or coupled Navier-type equation for displacement:

$$G\nabla^2 u_i + \frac{G}{1-2v} e_i - \alpha' p_i + \omega_0 \chi a C_i^{\mathrm{S}} = 0 \tag{9}$$

*Pressure Diffusion Equation*

Using conservation of mass for a weakly compressible fluid along with the expression for the flux, one obtains a coupled fluid diffusion equation.

$$\alpha \dot{\varepsilon}_{ii} + \left(Q' + B'\right)\dot{p} + \beta\chi a \dot{C}^{\mathrm{S}} - \frac{k}{\mu}\nabla^2 p + \frac{k\Re\,\bar{\rho}_{\mathrm{f}} a R T}{\mu c M^{\mathrm{S}}}\nabla^2 C^{\mathrm{S}} = 0 \tag{10}$$

*Equation for Solute Diffusion*

Substituting Eq. 8 into equation of conservation of solute mass in rock yields the following equation:

$$\phi\eta_j \dot{C}_j^{\mathrm{S}} + (1-\Re)\nabla\left(J_{\mathrm{f}} C_j^{\mathrm{S}}\right) - (1-\Re) D \nabla^2 C_j^{\mathrm{S}} = 0 \tag{11}$$

where $\eta$ is the solute retardation coefficient.

The last equation (solute transfer equation) as presented by Heidug and Wong (1996) and Ghassemi and Diek (2003) is as follows:

$$\phi \dot{C}_j^{\mathrm{S}} - D\nabla^2 C_j^{\mathrm{S}} + \nabla\left(J_{\mathrm{f}} C_j^{\mathrm{S}}\right) = 0 \tag{12}$$

However, Eq. 12 does not consider the efficiency of the membrane. Mass flow of solute used to derive the Eq. 12 is as follows:

$$J_{j\mathrm{s}} = \bar{\rho}_{\mathrm{f}} J_{\mathrm{f}} C_j^{\mathrm{S}} - \bar{\rho}_{\mathrm{f}} D \nabla C_j^{\mathrm{S}} \tag{13}$$

In order to account for the reflection coefficient of shale formation, Eq. 13 can be written similar to Eq. 8 (Lal 1999; Kooi and Garavito 2003):

On the other hand the solute mass conservation in porous media, where porosity and retardation coefficient are consider unchanged based on time, can be expressed as follows (Bear 1988):

$$\phi\eta_j \dot{C}_j^{\mathrm{S}} + \nabla J_{j\mathrm{s}} = 0 \tag{14}$$

Substituting Eq. 8 into Eq. 14 yields Eq. 11.

The retardation coefficient is extremely dependent on rock properties and rock ability to absorb the chemical species. Note that for the rock with no membrane properties and retardation effect, Eq. 11 reduces to traditional Fick's Law.

## Appendix B

Definition of matrices formed in finite element formulation

All matrices are defined as follows:

$$K = \int_{Ve} B^T D B \,\mathrm{d}V$$

$$A = \int_{Ve} B^T \alpha' m N_P \,\mathrm{d}V$$

$$W = \int_{Ve} B^T \chi\omega_0 a m N_{C^{\mathrm{S}}} \,\mathrm{d}V$$

$$S = \int_{Ve} N_P^T \left(Q' + B'\right) N_P \,\mathrm{d}V$$

$$\hat{M} = \int_{Ve} N_P^T \beta\chi a m N_{C^{\mathrm{S}}} \,\mathrm{d}V$$

$$M = \int_{Ve} N_{C^s}^T \phi \eta N_{C^s} \, \mathrm{d}V$$

$$H_{\mathrm{H}} = \int_{Ve} (\nabla N_P)^T (k/\mu)(\nabla N_P) \, \mathrm{d}V$$

$$D_{\mathrm{H}} = \int_{Ve} (\nabla N_P)^T L_{\mathrm{D}} (\nabla N_P) \, \mathrm{d}V$$

$$D_{\mathrm{D}} = \int_{Ve} (\nabla N_{C^s})^T (1 - \Re) D (\nabla N_{C^s}) dV - \int_{Ve} (\nabla N_{C^s})^T (1 - \Re) J_{\mathrm{f}} N_{C^s} \, \mathrm{d}V$$

*Ve* is the spatial area of the element, f is the external applied load, *B* is the strain displacement matrix, and the other parameters are the same as previously defined. $\vec{D}_e$ is the elastic modulus tensor.

## References


Bader S, Kooi H (2005) Modelling of solute and water transport in semi-permeable clay membranes: comparison with experiments. Adv Water Resour 28(3):203–214

Bear J (1988) Dynamics of fluids in porous media. Dover, New York

Biot M (1941) General theory of three-dimensional consolidation. J Appl Phys 12(2):155–164

Boroomand B, Zienkiewicz OC (1997) An improved REP recovery and the effectivity robustness test. Int J Numer Methods Eng 40:3247–3277

Chenevert ME (1970) Shale control with balanced-activity oil-continuous muds. SPE J Petrol Technol 22(10):1309–1316

Detournay E, Cheng AHD (1988) Poroelastic response of a borehole in a non-hydrostatic stress field. Int J Rock Mech Min Sci Geomech Abstr 25(3):171–182

Ekbote S, Abousleiman Y (2006) Porochemoelastic solution for an inclined borehole in a transversely isotropic formation. J Eng Mech 132(7):754–763

Ghassemi A, Diek A (1998) A solution for stress distribution around an inclined borehole in shale. Int J Rock Mech Min Sci 35(4–5):538–540

Ghassemi A, Diek A (2003) Linear chemo-poroelasticity for swelling shales: theory and application. J Petrol Sci Eng 38(3–4):199–212

Ghassemi A, Tao Q (2009) Influence of coupled chemo-poro-thermoelastic processes on pore pressure and stress distributions around a wellbore in swelling shale. J Petrol Sci Eng 67(1–2):57–64

Hanshaw BB, Zen E-A (1965) Osmotic equilibrium and overthrust faulting. Geol Soc Am Bull 76(12):1379–1385

Heidug WK, Wong S-W (1996) Hydration swelling of water-absorbing rocks: a constitutive model. Int J Numer Anal Methods Geomech 20(6):403–430

Hodge MO (2006) Avoiding wellbore failure by time dependent stability analysis of stressed poroelastic rocks. Petrol Eng. Sydney, New South Wales, 295

Kooi H, Garavito AM (2003) Numerical modelling of chemical osmosis and ultrafiltration across clay formations. J Geochem Explor 78–79:333–336

Lal M (1999) Shale stability: drilling fluid interaction and shale strength. SPE Asia Pacific oil and gas conference and exhibition. Jakarta, Indonesia, Society of Petroleum Engineers

Mody FK, Hale AH (1993) Borehole-stability model to couple the mechanics and chemistry of drilling-fluid/shale interactions. SPE J Petrol Technol 45(11):1093–1101

Muhammad N (2004) Hydraulic, diffusion, and retention characteristics of inorganic chemicals in bentonite. Dissertation, Civil Environ Eng, University of South Florida

Nguyen VX, Abousleiman YN (2009a) Poromechanics response of inclined wellbore geometry in chemically active fractured porous media. J Eng Mech 135(11):1281–1294

Nguyen VX, Abousleiman YN (2009b) Analyses of wellbore instability in drilling through chemically active fractured-rock formations. SPE J 14(2):283–301

Rice JR, Cleray MP (1976) Some basic stress diffusion solutions for fluid saturated elastic porous media with compressible constituents. Rev Geophys Space Phys 14:227–241

Shackelford CD (1990) Transit-time design of earthen barriers. Eng Geol 29(1):79–94

Sherwood JD (1993) Biot poroelasticity of a chemically active shale. Proc Math Phys Sci 440(1909):365–377

Sherwood JD, Bailey L (1994) Swelling of shale around a cylindrical wellbore. Proc Math Phys Sci 444(1920):161–184

van Oort E, Hale AH (1996) Transport in shales and the design of improved water-based shale drilling fluids. SPE Drill Compl 11(3):137–146

Zhang J, Roegiers JC (2005) Double porosity finite element method for borehole modeling. Rock Mech Rock Eng 38(3):217–242

Zienkiewicz OC, Taylor RL (2000) The finite element method, basic formulation and linear problems. Butterworth-Heinemann, Oxford

Zienkiewicz OC, Zhu JZ (1992) The superconvergence patch recovery and a posteriori error estimates, part I: the recovery techniques. Int J Numer Methods Eng 33:1331–1364

Zoppou C, Knight JH (1997) Analytical solutions for advection and advection-diffusion equations with spatially variable coefficients. J Hydraul Eng 123(2):144–148